Angewandte Chemie
Eine Zeitschrift der Gesellschaft Deutscher Chemiker

Supporting Information

Dynamically Resettable Electrode-Electrolyte Interface through Supramolecular Sol-Gel Transition Electrolyte for Flexible Zinc Batteries

P. Li, M. Liao, S. Cui, J. Li, L. Ye, Y. Yang, C. Wang, B. Wang, H. Peng**

SUPPORTING INFORMATION

Table of Contents

SUPPORTING INFORMATION

Experimental Procedures

Materials. Pluronic F-127 block copolymer ($PEO_{100}PPO_{65}PEO_{100}$, M_w=12600 g/mol) was obtained from BASF. α-cyclodextrin (α-CD, ≥98%), graphite (≥99%), zinc trifluoromethane sulfonate ($Zn(CF_3SO_3)_2$, RG, 99%), Manganese dioxide (MnO_2, SP) powder, and N, N-dimethylformamide (DMF, ≥99.8%) were purchased from Adamas. Manganese sulfate monohydrate ($MnSO_4·H_2O$, ≥99%) and Graphene (3000 mesh) were obtained from Sigma-Aldrich. Zinc powder (99.99%), zinc chloride ($ZnCl_2$, 98%), zinc acetate ($Zn(Ac)_2·2H_2O$, AR, 99%), and ultrahigh capacitance porous activated carbon (AC, 1800 $m^2·g^{-1}$, 5-8 μm) were purchased from Aladdin. Zinc sulfate heptahydrate ($ZnSO_4·7H_2O$, AR, ≥99%), sodium sulfate (Na_2SO_4, AR, ≥99%), and ammonium chloride (NH_4Cl, AR, ≥99.5%) were purchased from General-Reagent. Potassium sulfate (K_2SO_4, AR) was purchased from Sinopharm Chemical Reagent Co., Ltd. Thermoplastic polyurethane (TPU, 2792A) was obtained from Covestro. Conductive carbon black (Super P, 30-45 nm) was purchased from XFNANO material technology Co., Ltd. Polyaniline (PANI, AR) was purchased from Guangdong Haozhi Chemical Co., Ltd.

Synthesis of V_6O_{13}. V_6O_{13} nano-textiles were synthesized based on a previous facile solution-redox-based self-assembly method.[1] Specifically, α-MnO_2 power was soaked in the aqueous $VOSO_4$ solution with a concentration of 0.1 M overnight at room temperature, and a dark yellow suspension was obtained. In this redox process, MnO_2 was used as the oxidant and template, and VO^{2+} served as both the reducer and vanadium source. The resultant V_6O_{13} was collected by rinsing and centrifuging three times and then dried overnight in an oven.

Synthesis of sol-gel transition electrolyte (SGTE). SGTE consisted of the Pluronic F-127 polymer skeleton, electrolyte salt solution, and α-cyclodextrin. Since it was difficult for Pluronic to dissolve in water at room temperature, the SGTE polymer skeleton was prepared by dissolving Pluronic in an ice water bath. By changing the mixing ratio of Pluronic to water, the sol-gel transition temperature of electrolyte could be easily adjusted, and the sol-gel transition temperature decreased with the weight ratio of Pluronic to water increased. When the amount of Pluronic required to prepare was large, it was gradually dissolved a small number of times in an ice water bath. Mixing a small amount of Pluronic F-127 with 4 g of deionized water for each solution and stirring vigorously in an ice water bath for 2-4 hours until the required amount of Pluronic powder was completely dissolved. Furthermore, a specific amount of electrolyte salts and α-cyclodextrin were introduced into the electrolyte to adjust the gelation temperature, successively. By adjusting the types/concentrations of electrolyte salts and mass ratio of Pluronic/α-cyclodextrin/water, a flexible temperature-responsive SGTE with adjustable sol-gel transition temperature, high ionic conductivity, and excellent electrochemical performance could be achieved. Specifically, for $Zn(CF_3SO_3)_2$ SGTE used in the flexible Zn/V_6O_{13} battery and flexible Zn/AC hybrid supercapacitors, 55% (w/w) Pluronic was successively dissolved in 4 g deionized water in an ice water bath until the polymer was fully dissolved. Afterward 1 M $Zn(CF_3SO_3)_2$ was added to the above solution and stirred vigorously for 2 h. Then 12.5% (w/w) α-cyclodextrin powder was added and stirred for 1 h before ultrasonic for 10 min; the process was repeated three times. Finally, the SGTE was obtained by continuously stirring for 4 hours and standing for 12 hours under the ice water bath and at room temperature. For $ZnSO_4$ + $MnSO_4$ SGTE used in flexible Zn/MnO_2 battery, 25% (w/w) Pluronic was dissolved in 4 g deionized water in an ice water bath until the mixed solution became clear and transparent. Then 0.6 M $ZnSO_4$ + 0.05 M $MnSO_4$ was introduced into the above solution and stirred in an ice water bath for 1 h. Finally, 2.25% (w/w) α-cyclodextrin powder was added and stirred for 1 h and ultrasonic for 10 min, repeated this process three times and the SGTE was obtained by continuous stirring for 4 hours and standing for 12 hours under an ice water bath and at room temperature, respectively. For $ZnCl_2$ SGTE used in the flexible Zn/PANI battery, except that the Pluronic mass percentage became 30% (w/w), the concentration of $ZnCl_2$ is 3 M, and the mass percentage of α-cyclodextrin was 3% (w/w), other conditions were the same. These gels were freeze-dried to give polypseudorotaxane powder for further characterization.[2]

Preparation of electrode slurry. The modified electrode slurries for printing flexible batteries were prepared according to previous literature.[3] A certain amount of thermoplastic polyurethane (TPU) resin was added into the N, N-dimethylformamide (DMF) solvent and heated to 85 °C, then stirred for 2 h until it was completely dissolved. Afterward, graphite, graphene, super P, and electrode active materials (Zn powder, MnO_2 powder, V_6O_{13} powder, PANI powder, and AC powder) were successively added to the above solution and stirred vigorously at room temperature for 2 h. In this way, electrode slurries with different compositions and functions were achieved, in which the viscosity could be easily adjusted by changing the TPU or solid content. Specifically, for carbon-based conductive slurry, the mass percentage of TPU, graphite, graphene, and super P was 8%, 17%, 25%, and 50%, respectively. For Zn anode slurry, the mass percentage of TPU, graphite, graphene, super P, and Zn powder was 4%, 5%, 6%, 15%, and 70%, respectively. For MnO_2, V_6O_{13}, PANI, and AC cathode slurry, the mass percentage of TPU, graphite, graphene, super P, and cathode active material was 4%, 9%, 12%, 25%, and 50%, respectively.

Preparation of flexible electrodes. The flexible planar interdigitated electrodes were prepared by screen-printing.[4] First, the as-prepared graphene conductive slurry was added onto the pre-customized precision screen mesh placed above the polyethylene terephthalate (PET) flexible substrate. Then a rubber squeegee was swept across the surface of the screen at a suitable speed and with sufficient force to penetrate conductive slurry through a patterned screen onto the substrate. Then the electrode was placed in a vacuum oven and dried at 80 °C for 4 h to remove excess solvent. Afterward, the screen was replaced by another customized screen, and the Zn anode slurry and cathode slurry (V_6O_{13}, MnO_2, PANI, and AC) were screen-printed on graphene current collectors successively. Finally, the flexible electrodes with interdigitated architecture were obtained after it was fully dried in a vacuum oven at 80 °C for 12 h and cut into a rectangle with scissors.

SUPPORTING INFORMATION

Assembly of flexible battery. To facilitate subsequent electrochemical tests, the conductive copper foil was pasted on the anode and cathode to lead electrodes, and the commercial conductive silver glue (SC666-80R, Uniwell) was used to bond the connection between the copper foil and carbon-based electrode. The flexible electrode was dried in an oven at 80 °C to solidify the conductive silver glue. After that the SGTE prepared in advance was placed in a 0 °C cryogenic box for 3 minutes to fully complete the gel-sol transition, and then the SGTE with sol state was evenly coated on the surface of the flexible electrode and stood at room temperature for 10 minutes to fully complete the sol-gel transition. Finally, a transparent plastic film was used to wrap the flexible battery to obtain the dynamically resettable flexible batteries with interdigitated architecture. The overall size of the battery was about 40 cm^2 and its specific capacity was calculated based on the mass of cathode active material. The normalized mass loading of active materials was controlled at 1.0-1.5 $mg \cdot cm^{-2}$ by an electronic macro-balance (BT25S, 0.0001 mg).

Electrochemical measurement. Cyclic voltammetry (CV) measurements of flexible batteries were carried out by the CHI660E electrochemical workstation with scan rates ranging from 0.1-1.0 $mV \cdot s^{-1}$ versus Zn/Zn^{2+}. The electrochemical impedance spectroscopy (EIS) was conducted from 0.1 MHz to 10 mHz with a potential amplitude of 5 mV. Galvanostatic charge-discharge (GCD) profiles, plating-stripping profiles, and cycling life measurements were taken from the LAND CT2001A battery test system (Wuhan Land Electronic Co., Ltd, China). Zn//Zn symmetric cells were used for plating-stripping tests in CR2032 coin cells. The cell tested at gel and sol states was achieved by keeping batteries at room temperature (30 °C) or in a 0 °C cryogenic box, which could keep a constant temperature environment. Temperature-dependent electrochemical tests were achieved by placing batteries on a heating stage to control temperatures ranging from 20 to 70 °C. For Zn//Zn symmetric batteries, two pieces of metallic Zn foil were used as cathode and anode, respectively. For Zn//stainless steel asymmetric batteries, metallic Zn foil and stainless steel were used as anode and cathode, respectively. The glass fiber with 1 M zinc trifluoromethane sulfonate ($Zn(CF_3SO_3)_2$) SGTE or liquid electrolyte was used as a separator in the CR2032 coin cell. The dosage of electrolytes was controlled to be 40-60 μL. A fixed charging/discharging time of 1h was used for all galvanostatic charge-discharge measurements of Zn//Zn cells at different current densities. The ionic conductivities of SGTEs were measured by sandwiching electrolytes between two stainless steel (SS) foil (1 cm×1 cm) blocking electrodes over a frequency range of 1 MHz to 100 mHz with 10 mV AC amplitude. The following equation is used to estimate the ionic conductivity:[5]

$\sigma = l/(R_b \cdot A)$

Where σ is ionic conductivity ($S \cdot cm^{-1}$), l is the distance between the two stainless steel electrodes, R_b is the ohmic resistance of the electrode, and A is the electrode area.

Characterizations. The microstructure and morphology of the Pluronic, Zn anode, and SGTE coated electrode were characterized by cryo field-emission scanning electron microscopy (Zeiss Gemini SEM500 FESEM) with an accelerating voltage of 3.0 kV, which is also equipped with energy-dispersive spectrometer (EDS) detector to determine the composition and distribution of the element. The thermal stability property of SGTE was recorded with a Thermogravimetric analyzer (Pyris 1, TGA) from 20 to 600 °C at a rate of 20 $°C \cdot min^{-1}$ in the N_2 atmosphere. X-ray diffraction (XRD) patterns were recorded in a Burker-AXS with Cu-$K_{\alpha 1}$ radiation. ^1H nuclear magnetic resonance (NMR) spectra were recorded at room temperature on a Bruker ARX 400 NMR instrument with DMSO-d_6 as solvent (AVANCE III HD). The rheological properties of SGTEs were investigated with a rotary rheometer (HAAKE MARS III). The contact angle measurements were performed using an OCA20 contact angle meter (data physics, Germany). Photographs were taken with a digital camera (SONY A6000, Japan).

Results and Discussion

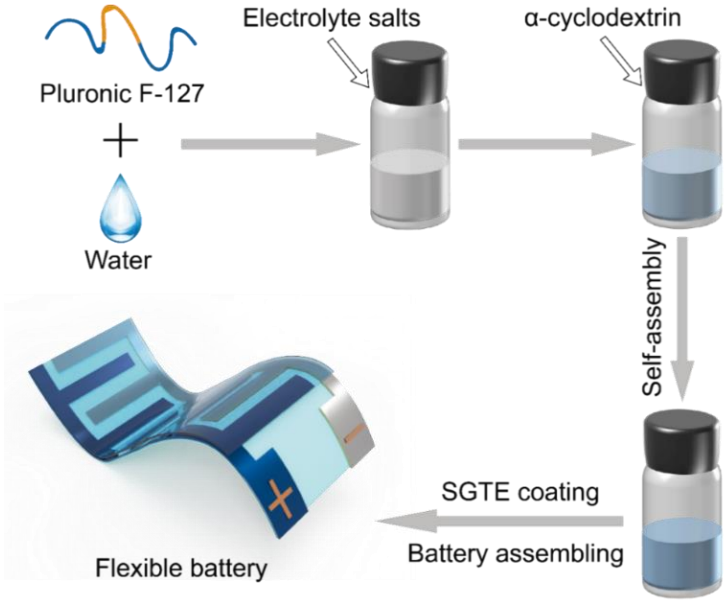

Figure S1. Diagram of preparation process of SGTE for flexible batteries.

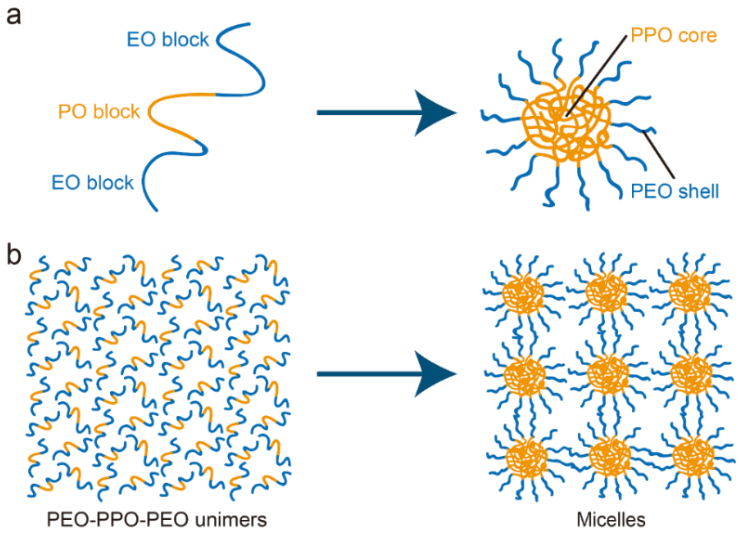

Figure S2. Pluronic and corresponding self-assembled micelle morphology.

Physical thermo-responsive polymer hydrogels are usually physical crosslinking networks formed by the physical entanglement of polymer chains or non-covalent bond interactions.[6] Pluronic exhibits a typical sol-gel (or gel-sol) transition as the temperature rises (or falls). This is because Pluronic is highly soluble and exists as unimers in water at low temperatures, so the system behaves as a fluid sol state on the macroscale. When the ambient temperature rises above the critical micelle temperature (CMT), the hydrophobicity of PPO increases, and block copolymers in the solution are driven to self-assemble into micelles with hydrophilic PEO segments as “shells” and hydrophobic PPO segments as “cores”. As temperature further increases and micelles are densely packed, the system is difficult to flow, showing the sol-gel transition.

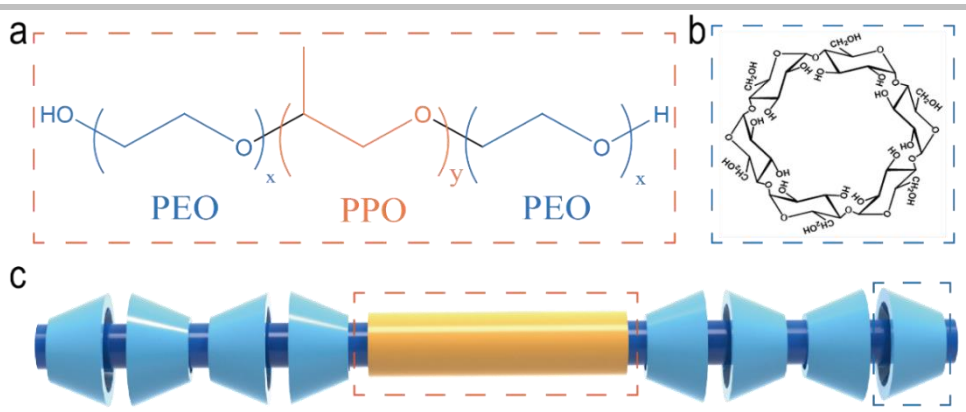

Figure S3. Structures of (**a**) Pluronic, (**b**) α-CD, and (**c**) pseudopolyrotaxane.

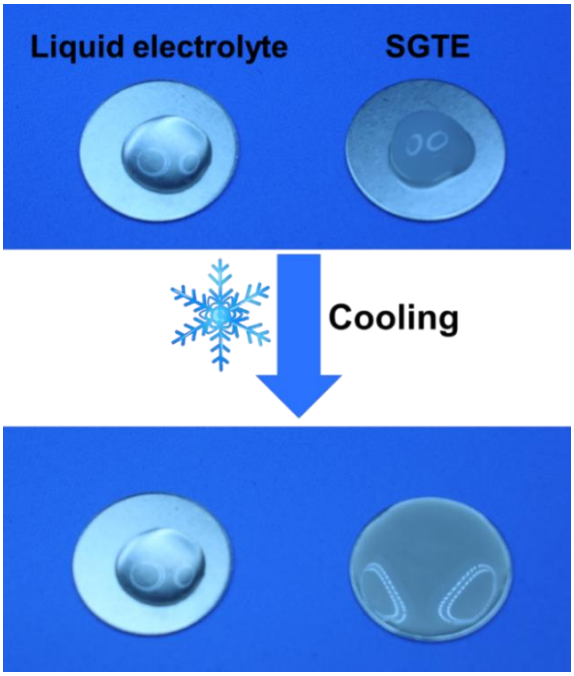

Figure S4. Wetting behaviors of SGTE and liquid electrolyte (1 M $Zn(CF_3SO_3)_2$) on a freezing stainless steel plate.

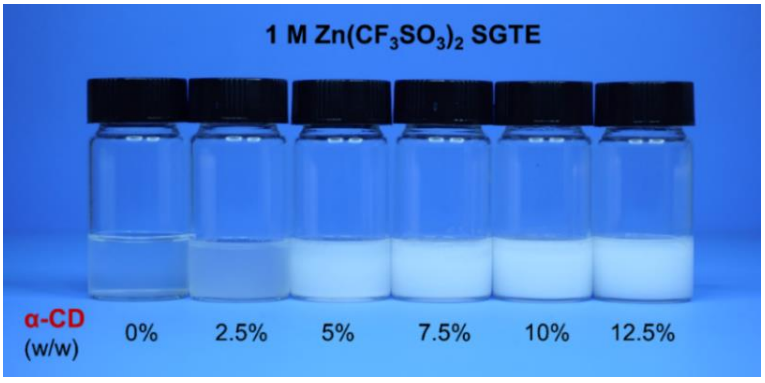

Figure S5. Photographs of SGTE with 1 M $Zn(CF_3SO_3)_2$ and different α-CD contents ranging from 0 to 12.5% (w/w).

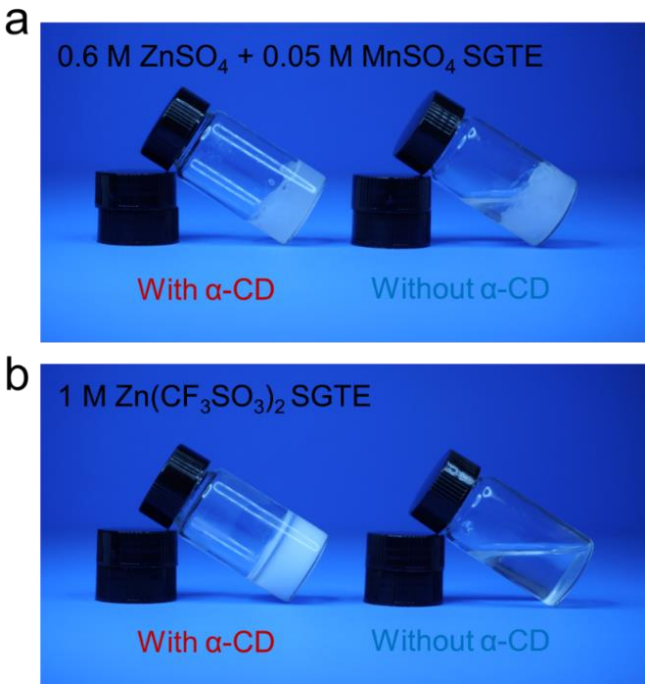

Figure S6. Photographs of (**a**) 0.6 M $ZnSO_4$ + 0.05 M $MnSO_4$ and (**b**) 1 M $Zn(CF_3SO_3)_2$ SGTEs with and without α-CD.

The addition of salt affects the apparent hydrophobicity of the polymer.[7] Salt-out ions (such as SO_4^{2-}) make Pluronic more hydrophobic and increase the number of micelles, resulting in dense micelle accumulation at lower temperatures and a decrease in gelation temperature. Salt-soluble ions (such as $CF_3SO_3^-$) make Pluronic more hydrophilic, resulting in fewer micelles and less dense accumulation at the same temperature. On the macroscale, the gelation temperature increased and SGTE kept sol at room temperature, and adding α-CD can contain high concentrations of salt ions to reduce gelation temperature.

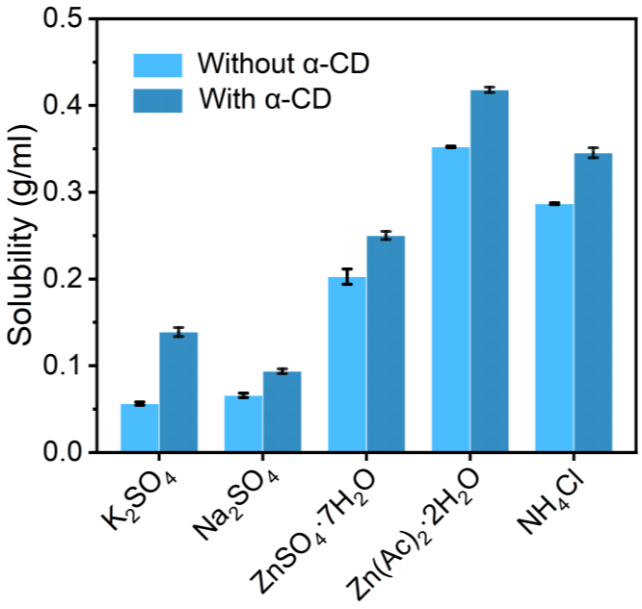

Figure S7. Solubilities of K_2SO_4, Na_2SO_4, $ZnSO_4 \cdot 7H_2O$, $Zn(Ac)_2 \cdot 2H_2O$, and NH_4Cl in SGTEs (25 wt% Pluronic solutions) with 3 wt% α-CD or without α-CD at room temperature.

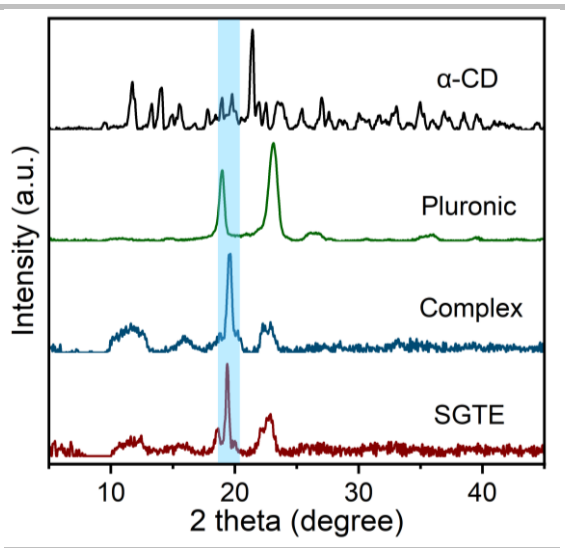

Figure S8. X-ray diffraction patterns of α-CD, Pluronic F-127, pseudopolyrotaxane complex, and $Zn(CF_3SO_3)_2$ SGTE.

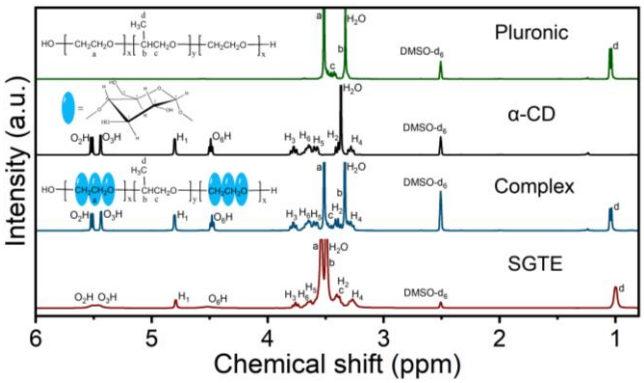

Figure S9. ^1H nuclear magnetic resonance spectra of Pluronic F-127, α-CD, polypseudorotaxane complex, and 1 M $Zn(CF_3SO_3)_2$ SGTE in DMSO-d_6.

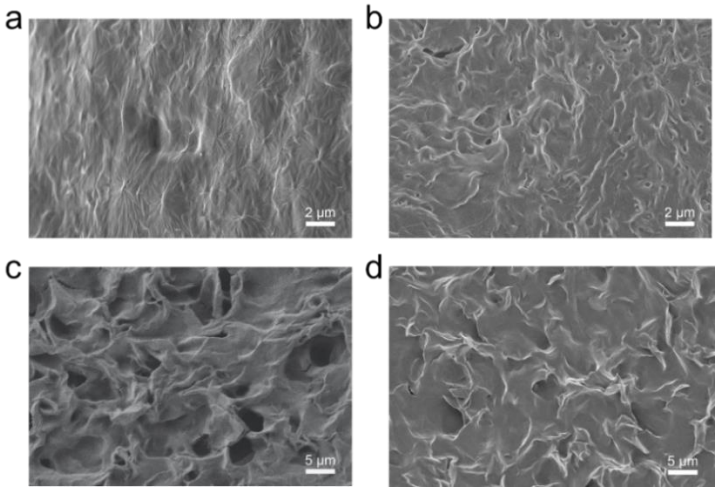

Figure S10. Scanning electron microscopy images of Pluronic and pseudopolyrotaxane complex (**a**, **c**) after freeze-dried and (**b**, **d**) evaporated at room temperature.

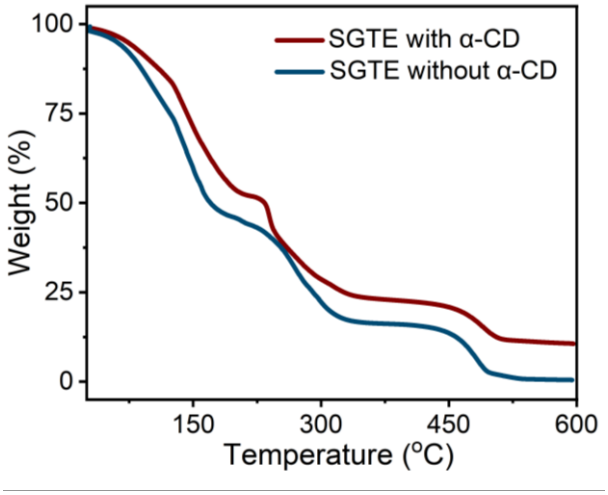

Figure S11. Thermogravimetric analysis curves of the gel state 1 M $Zn(CF_3SO_3)_2$ SGTE with and without α-CD addition.

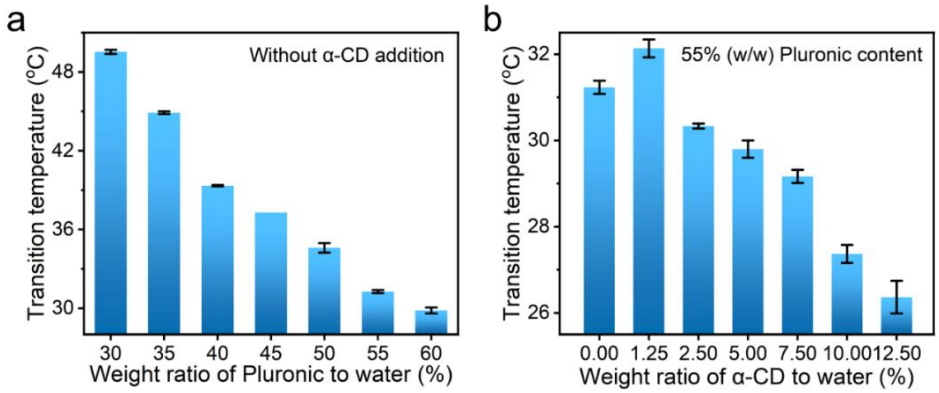

Figure S12. Relationship of sol-gel transition temperature with the weight ratio of (**a**) Pluronic and (**b**) α-CD to water.

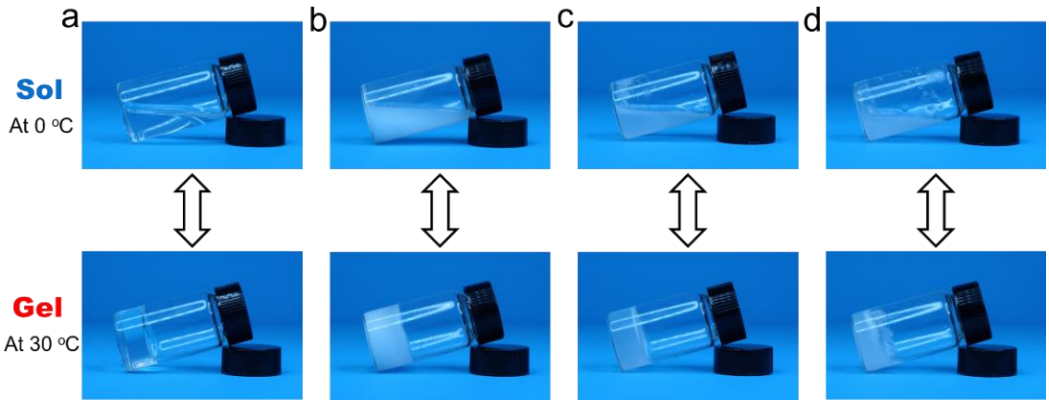

Figure S13. Photographs of different reversible SGTEs. (**a**) Pure Pluronic F-127 solution with a polymer concentration of 20% (w/w). (**b**) 1 M $Zn(CF_3SO_3)_2$, (**c**) 3 M $ZnCl_2$, and (**d**) 0.6 M $ZnSO_4$ + 0.05 M $MnSO_4$.

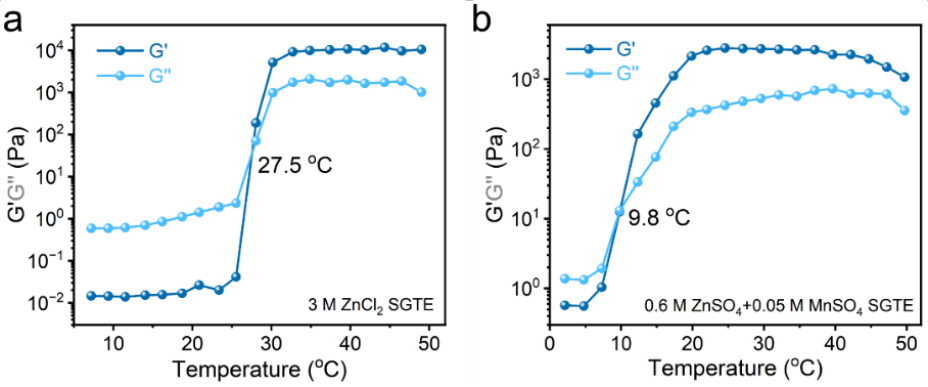

Figure S14. Sol-gel transition behaviors of (**a**) 3 M $ZnCl_2$ SGTE, (**b**) 0.6 M $ZnSO_4$ + 0.05 M $MnSO_4$ SGTE.

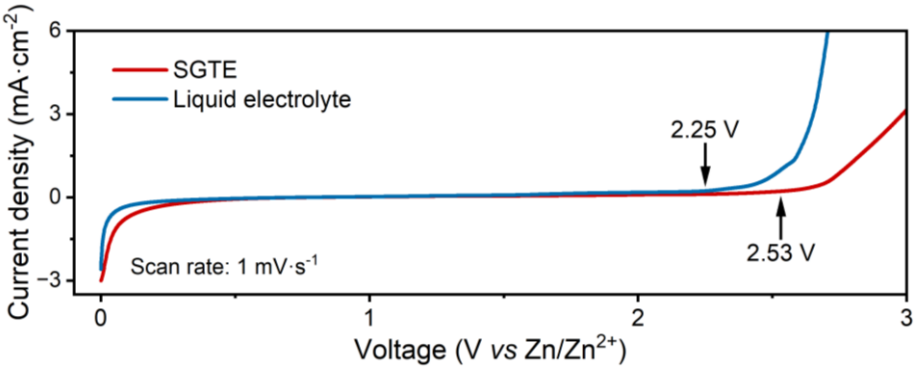

Figure S15. Linear sweep voltammetry curves of 1 M $Zn(CF_3SO_3)_2$ SGTE and corresponding liquid electrolyte.

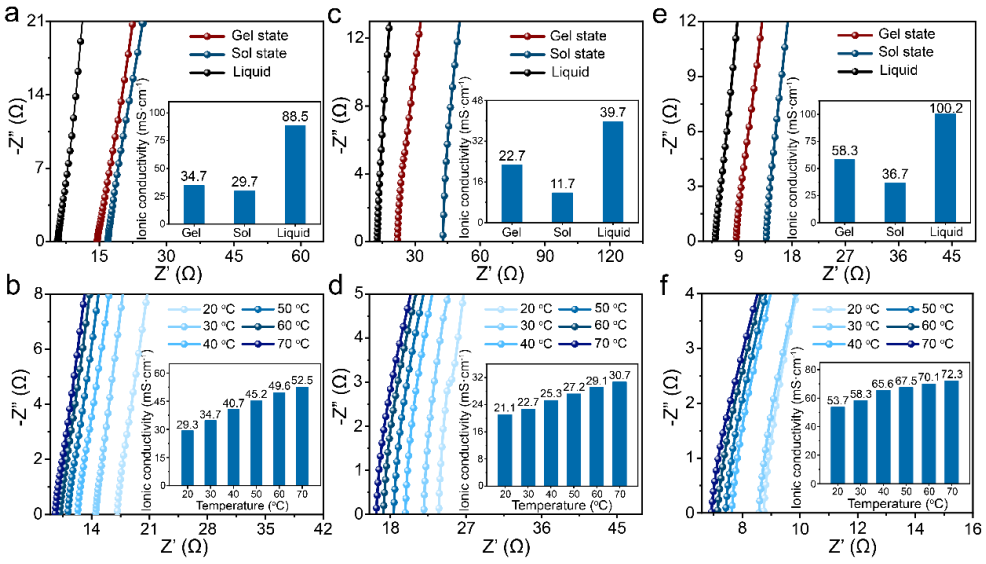

Figure S16. Nyquist impedance plots and corresponding ionic conductivities of SGTEs with (**a**, **b**) 1 M $Zn(CF_3SO_3)_2$, (**c**, **d**) 0.6 M $ZnSO_4$ + 0.05 M $MnSO_4$, and (**e**, **f**) 3 M $ZnCl_2$ at various states and temperatures.

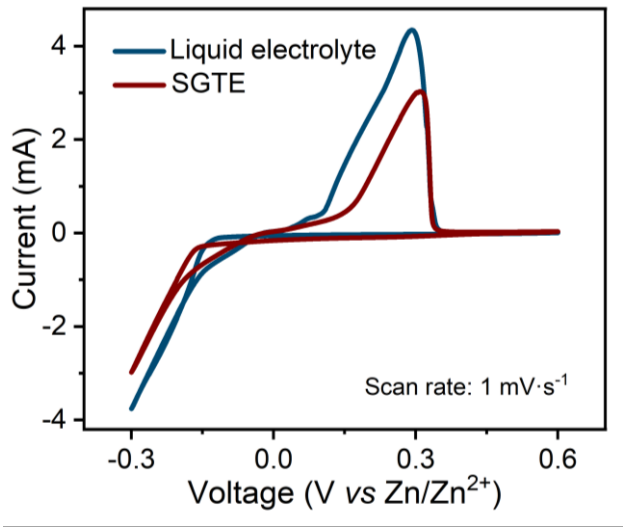

Figure S17. Cyclic voltammetry curves of Zn deposition/dissolution.

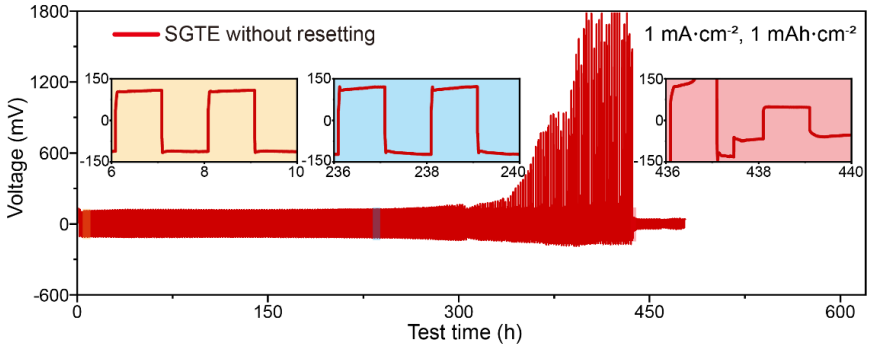

Figure S18. Voltage profiles of Zn//Zn symmetric cell based on 1 M $Zn(CF_3SO_3)_2$ SGTE without resetting at 1 mA·cm^2 and 1 mAh·cm^2.

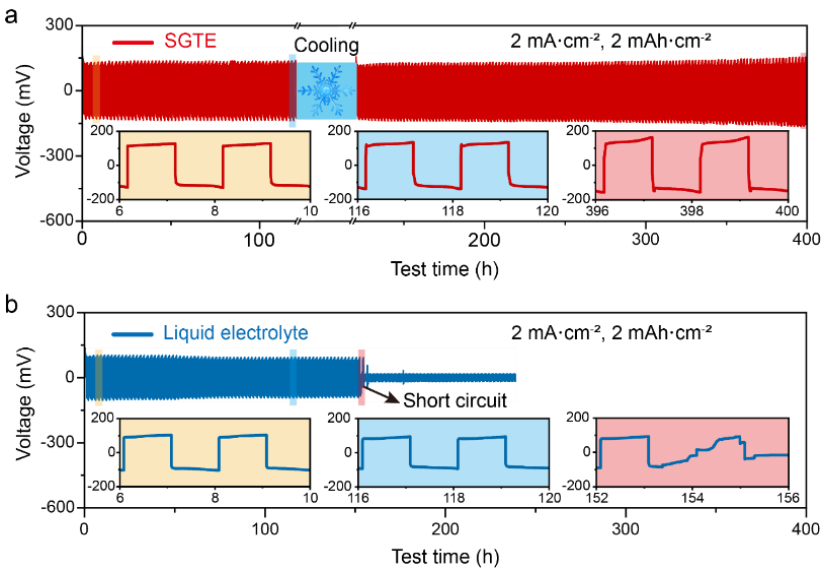

Figure S19. Voltage profiles of Zn//Zn symmetric cells based on 1 M $Zn(CF_3SO_3)_2$ (**a**) SGTE with the resetting process and (**b**) liquid electrolyte at 2 mA·cm^{-2} and 2 mAh·cm^{-2}.

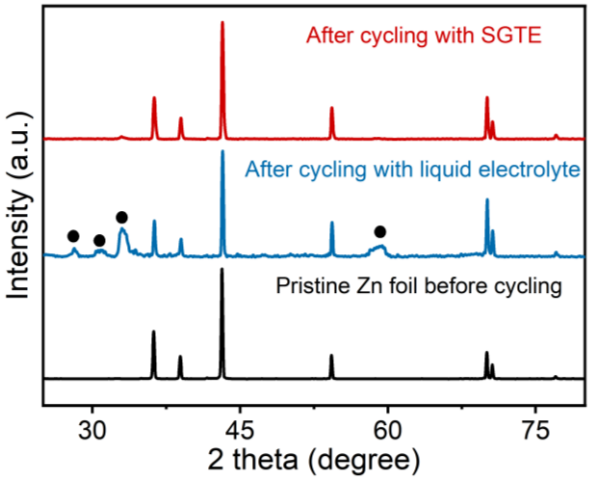

Figure S20. X-ray diffraction patterns of pristine Zn foil before cycling, Zn foil after cycling with 1 M $Zn(CF_3SO_3)_2$ liquid electrolyte and SGTE.

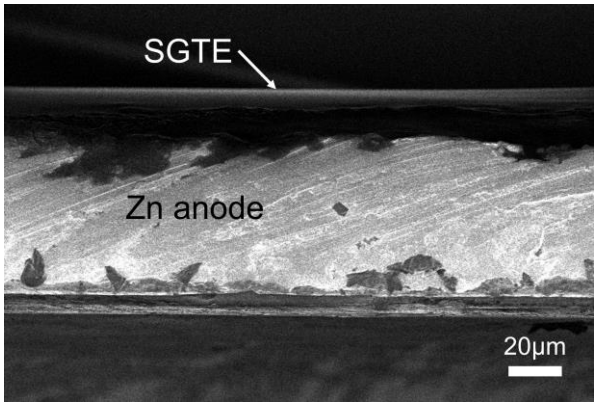

Figure S21. Cross-sectional scanning electron microscopy image of Zn foil fully wetted with 1 M $Zn(CF_3SO_3)_2$ SGTE.

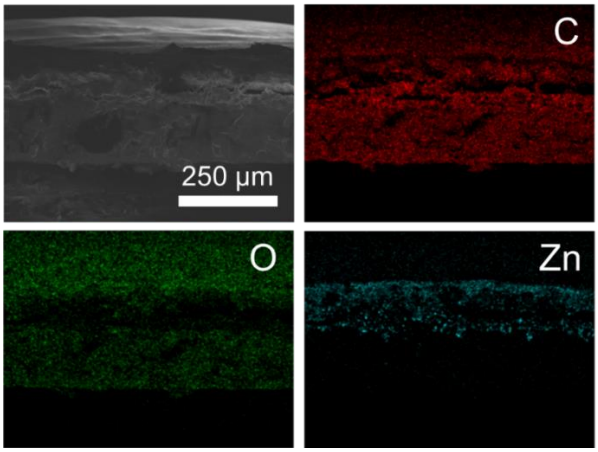

Figure S22. Cross-sectional scanning electron microscopy image and corresponding energy-dispersive spectrometer results of the printed flexible Zn anode fully wetted by 1 M $Zn(CF_3SO_3)_2$ SGTE.

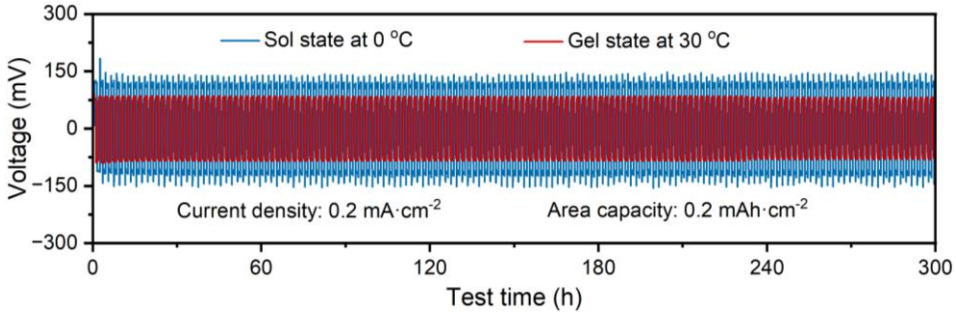

Figure S23. Voltage profiles of Zn plating-stripping in 1 M $Zn(CF_3SO_3)_2$ SGTE at sol (0 °C) and gel (30 °C) states.

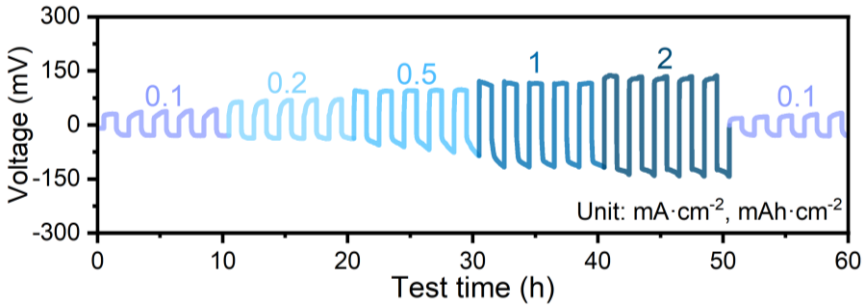

Figure S24. Rate cycling of Zn//Zn symmetric cell with 1 M $Zn(CF_3SO_3)_2$ SGTE at gel state (30 °C).

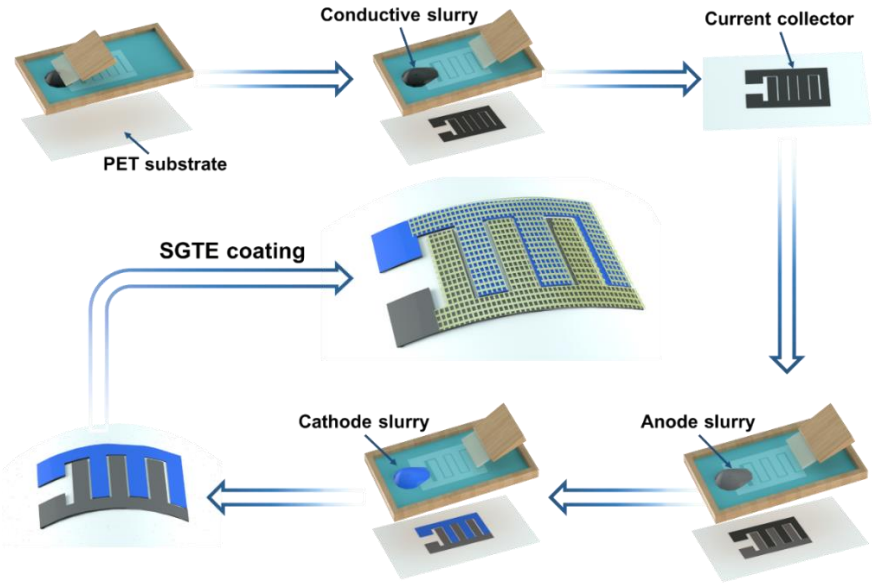

Figure S25. Schematic of the preparation procedures of flexible batteries *via* screen printing.

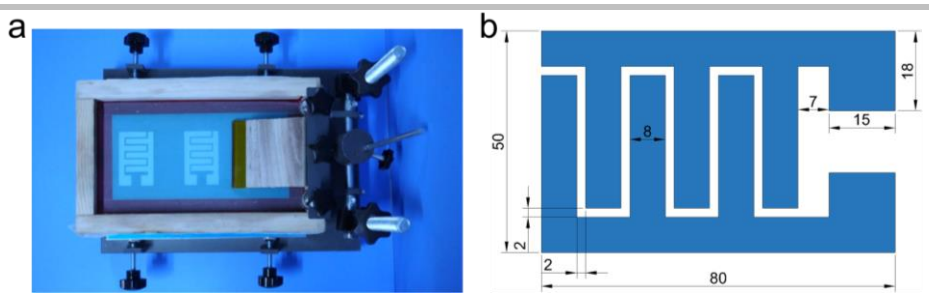

Figure S26. (**a**) Photograph of the screen-printing device and (**b**) detailed parameters of the flexible battery (unit, mm).

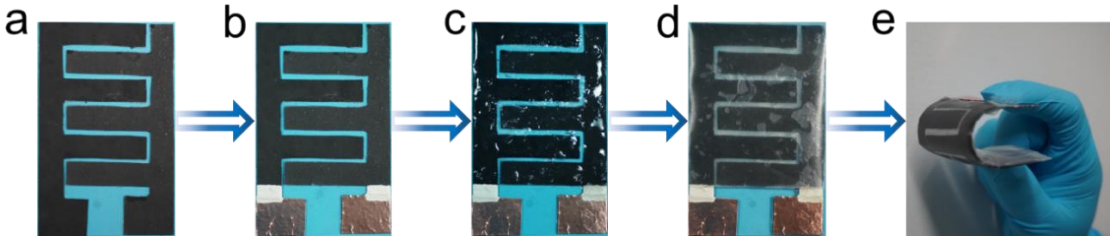

Figure S27. Photographs of flexible batteries at (**a**) electrodes printed, (**b**) Cu foil pasted, (**c**) SGTE coated, (**d**) transparent plastic film packaged, and (**e**) bending state.

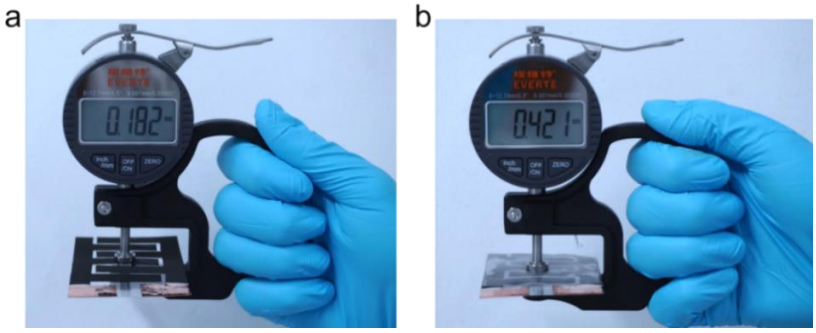

Figure S28. Photographs of the thickness of interdigital flexible battery with (**a**) electrodes printed, (**b**) SGTE-coated and plastic film packaged.

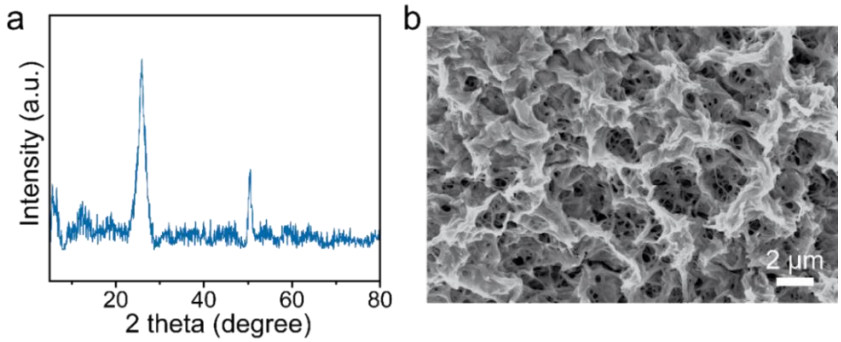

Figure S29. (**a**) X-ray diffraction pattern of as-prepared V_6O_{13} and (**b**) corresponding scanning electron microscopy image, indicating successful synthesis of V_6O_{13} cathode material.[1]

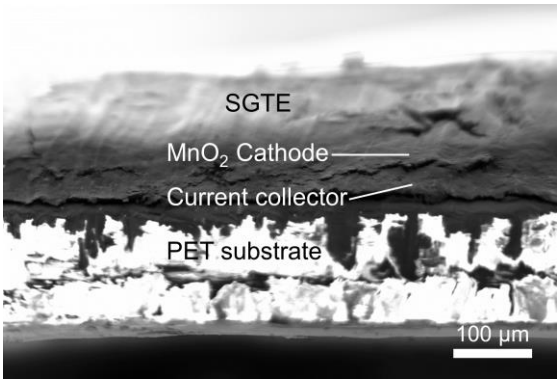

Figure S30. Cross-sectional scanning electron microscopy image of the printed flexible MnO_2 cathode fully wetted by 1 M $Zn(CF_3SO_3)_2$ SGTE.

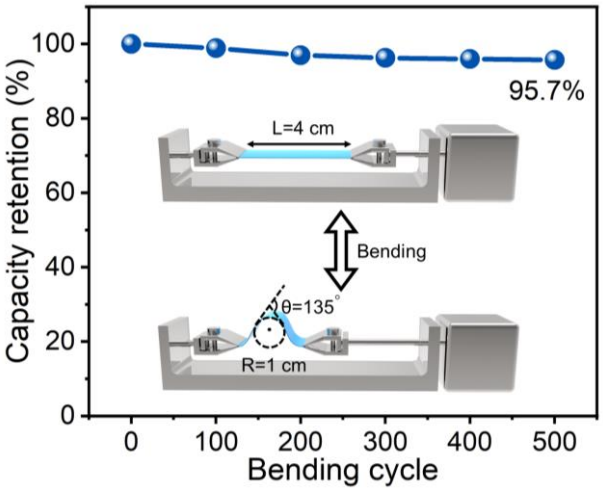

Figure S31. Dependence of capacity retention on bending cycle. The flexible Zn/V_6O_{13} battery with 1 M $Zn(CF_3SO_3)_2$ SGTE was continuously bent for 100 cycles, and the specific capacity was recorded after a cooling/resetting process.

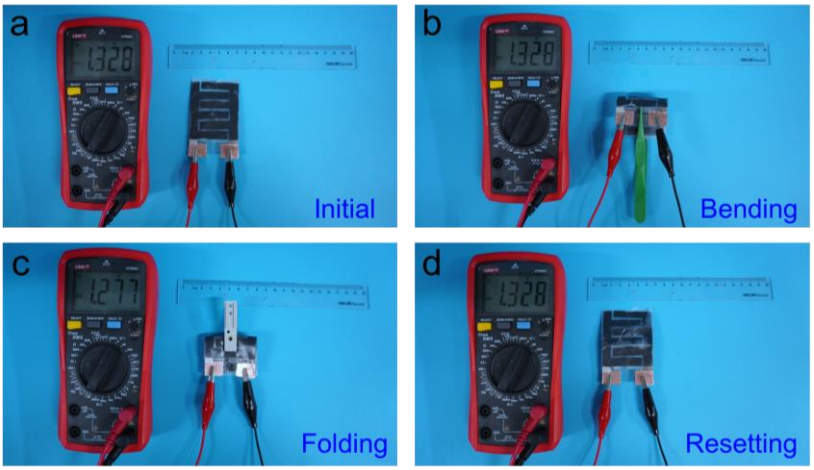

Figure S32. Open-circuit voltages of flexible $Zn/SGTE/V_6O_{13}$ battery under different states. (**a**) initial state, (**b**) bending state, (**c**) intensive folding state, and (**d**) after resetting state.

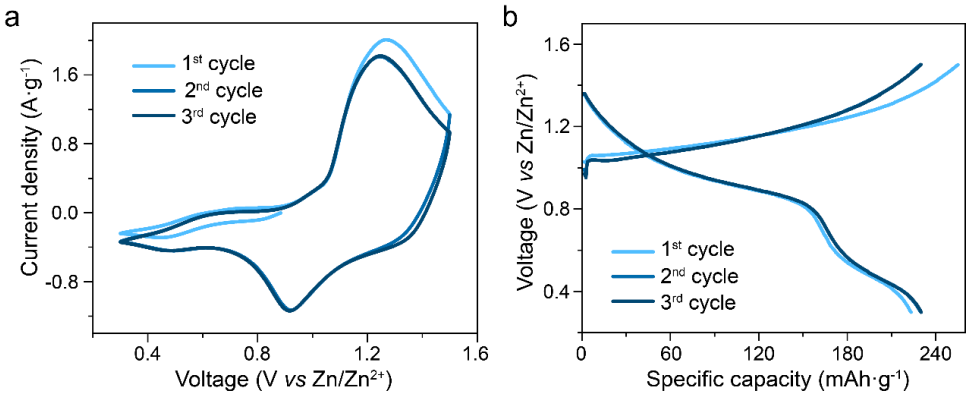

Figure S33. (**a**) Cyclic voltammetry and (**b**) galvanostatic charge-discharge curves of the first three cycles of flexible Zn/V_6O_{13} battery with 1 M $Zn(CF_3SO_3)_2$ SGTE at gel state at 1 $mV \cdot s^{-1}$ and 0.2 $A \cdot g^{-1}$.

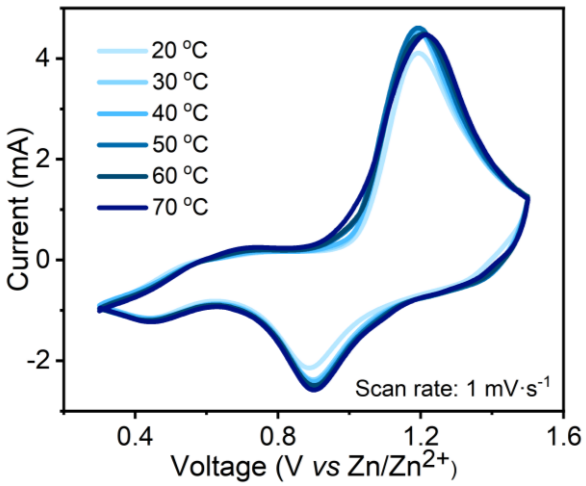

Figure S34. Cyclic voltammetry curves of flexible Zn/V_6O_{13} battery with 1 M $Zn(CF_3SO_3)_2$ SGTE at different temperatures.

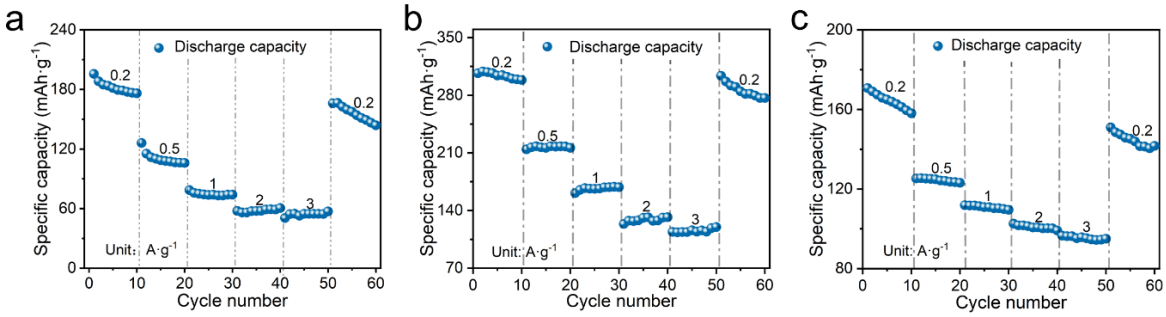

Figure S35. Rate performance of the flexible (**a**) Zn/MnO_2 battery based on 0.6 M $ZnSO_4$ + 0.05 M $MnSO_4$ SGTE, (**b**) Zn/V_6O_{13} battery based on 1 M $Zn(CF_3SO_3)_2$ SGTE, and (**c**) Zn/PANI battery based on 3 M $ZnCl_2$ SGTE.

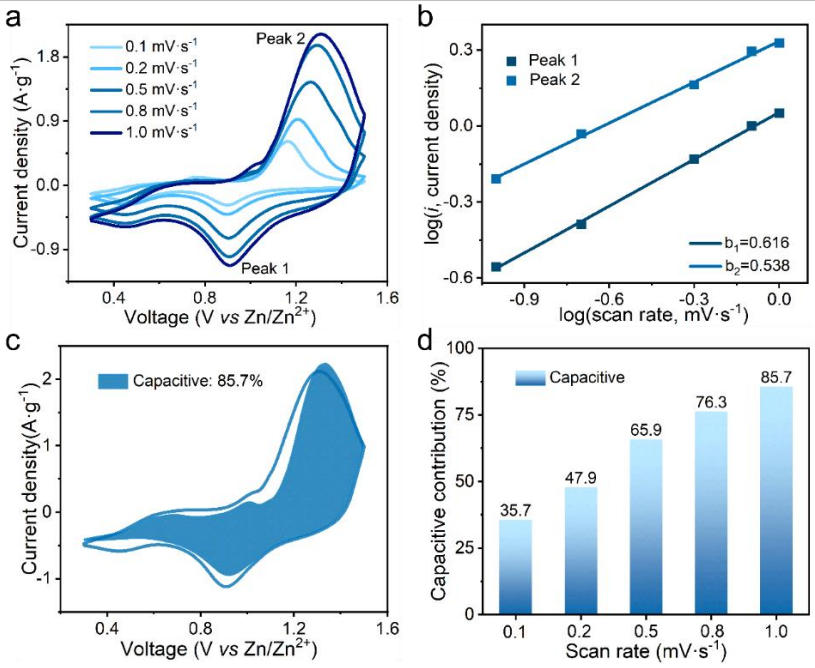

Figure S36. Electrode reaction kinetics analysis of flexible Zn/SGTE/V_6O_{13} battery. (**a**) Cyclic voltammetry curves at increasing scan rates ranging from 0.1 to 1.0 mV·s^{-1}. (**b**) Plots of log(*i*) versus log(*v*) of the cathodic current response at the typical two peaks labeled in (**a**). The slopes of fitted lines determine the b values. (**c**) Cyclic voltammetry displaying the capacitive contribution (blue region) to the total current at 1.0 mV·s^{-1}. (**d**) Percentages of capacity contributions at increasing scan rates. The corresponding discussion is provided in **Note S1**.

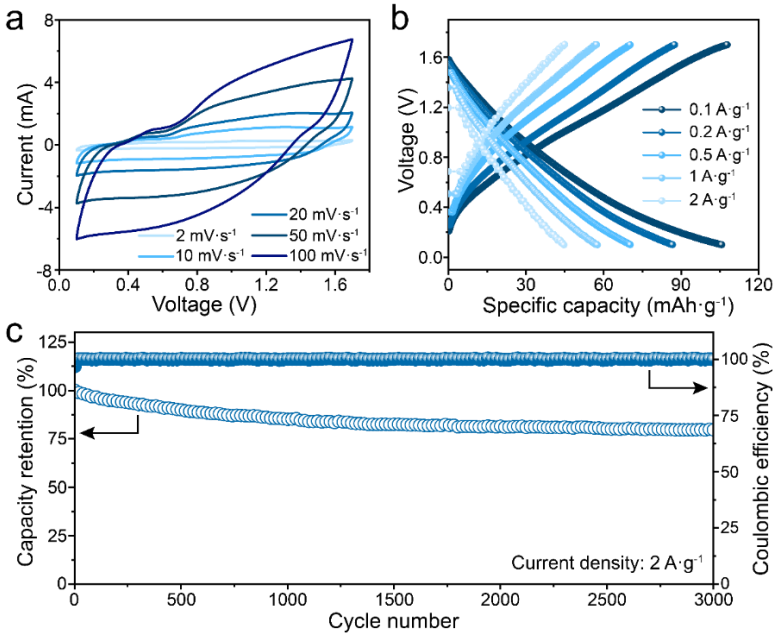

Figure S37. Electrochemical performances of flexible Zn/AC hybrid supercapacitors with 1 M $Zn(CF_3SO_3)_2$ SGTE. (**a**) Cyclic voltammogram. (**b**) Galvanostatic charge-discharge. (**c**) Cycling performance at 2 A·g^{-1}.

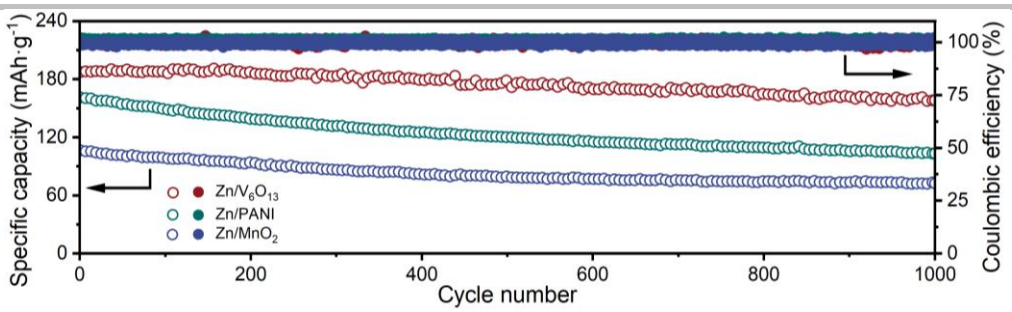

Figure S38. Cycling performance of flexible Zn/V_6O_{13}, Zn/PANI, and Zn/MnO_2 batteries with corresponding SGTEs in terms of specific capacity and corresponding coulombic efficiency at 1.0 $A \cdot g^{-1}$.

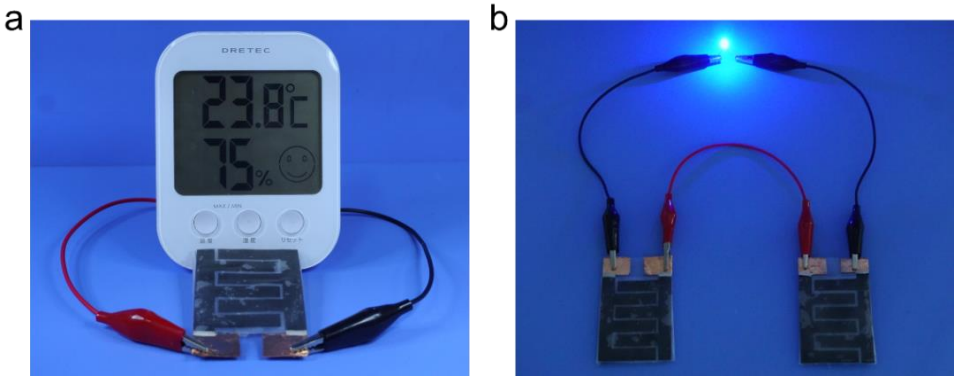

Figure S39. Photographs of (**a**) a digital temperature and humidity meter powered by a flexible $Zn/SGTE/MnO_2$ battery and (**b**) a light-emitting diode illuminated by two batteries in series.

Note S1. Cyclic voltammetry study of the flexible $Zn/SGTE/V_6O_{13}$ battery.

Taking flexible Zn/V_6O_{13} batteries coated by 1 M $Zn(CF_3SO_3)_2$ SGTE as an example, we studied the electrode reaction kinetics of assembled flexible batteries. The cyclic voltammetry curves of flexible Zn/V_6O_{13} batteries at increasing scan rates from 0.1 to 1.0 $mV \cdot s^{-1}$ within a voltage window from 0.3 to 1.5 V were shown in **Figure S36** (**a**). Two pairs of redox peaks could be observed in cyclic voltammetry curves. The capacitive effect of the battery system can be calculated using the relation $i = a \cdot v^b$. The relationship between the peak current densities (i) and scan rates (v) was assumed to follow this equation:[8]

$i=a \cdot v^b$,

where a and b were adjustable parameters. For analytical purposes, it could also be rearranged as the equation below:

$log(i)=blog(v) + log(a)$,

where b represented the slope of $log(i)$ versus $log(v)$ curve. When b approaches 0.5, faradic intercalation dominates the process; when the b value is close to 1.0, a capacitive response is indicated. Peak 1 and Peak 2 were selected as the typical indicators for the kinetics analysis of the flexible $Zn/SGTE/V_6O_{13}$ battery. By fitting the plots of $log(i)$ versus $log(v)$, the b values of Peak 1 and Peak 2 in cyclic voltammetry curves were calculated to be 0.616 and 0.538, respectively (**Figure S36** (**b**)). The obtained b values were both in the range of 0.5 to 1, suggesting that the charge and discharge processes of flexible zinc batteries were synchronously controlled by the capacitive and diffusion behaviors,[1b] which leads to fast Zn^{2+} diffusion kinetics and thus enabling the high-rate performance.

Furthermore, the capacitive contribution can be quantified by separating the current (i) at a fixed potential (V) into capacitive effect (k_1v) and diffusion-controlled insertion ($k_2v^{1/2}$), according to the below equation:[8]

$i=k_1v + k_2v^{0.5}$

which could also be represented as the equation:

$i/v^{0.5} =k_1v^{0.5} + k_2$

where i, k_1v, and $k_2v^{0.5}$ represented the current response, capacitive, and ionic diffusion contribution, respectively. The k_1 value could be obtained by fitting the $i/v^{0.5}$ versus $v^{0.5}$ plots, **Figure S36** (**c**) depicted the typical cyclic voltammetry profile at a scan rate of 1 $mV \cdot s^{-1}$ for the capacitive current (blue region) compared with the total current, and the capacitive contribution in the flexible battery was calculated to be 85.7%. Upon the decreasing scan rates, the percentages of capacitive contribution accordingly decreased to 76.3%, 65.9%, 47.9%, and 35.7% at scan rates of 0.8, 0.5, 0.2, and 0.1 $mV \cdot s^{-1}$, respectively (**Figure S36** (**d**)). The above results indicated that the flexible batteries showed facilitated charge transfer kinetics.

Table S1. Electrochemical performances of the SGTE-based flexible battery in comparison to other reported gel or polymeric electrolytes for zinc-ion batteries.

Gel electrolyte	Cathode material	Ionic conductivity	Specific capacity	Cycling performance	Flexibility	Ref.
1 M $Zn(CF_3SO_3)_2$ SGTE	**V_6O_{13}**	**34.7 mS·cm^{-1}**	**413 mAh·g^{-1} at 0.1 A·g^{-1}**	**199 mAh·g^{-1} after 600 cycles at 0.5 A·g^{-1}**	**95.7% capacity retention after bending 500 cycles**	**This work**
1 M $Zn(CF_3SO_3)_2$ gelatin-g-PAM	$Zn_3[Fe(CN)_6]_2$	2.04 mS·cm^{-1}	62 mAh·g^{-1} at 2.5 C	~50 mAh·g^{-1} after 260 cycles at 2.5 C	94.6% capacity retention after stitching 30 cycles	[9]
2 M $ZnSO_4$ + 0.1 M $MnSO_4$ PAM	MnO_2/CNT	16.5 mS·cm^{-1}	260.4 mAh·g^{-1} at 0.2 A·g^{-1}	101 mAh·g^{-1} after 500 cycles at 2 A·g^{-1}	93.6% capacity retention after bending 300 cycles	[10]
2 M $ZnSO_4$ + 0.2 M $MnSO_4$ NFC/PAM	MnO_2/CNT	22.8 mS·cm^{-1}	307 mAh·g^{-1} at 1 C	190 mAh·g^{-1} after 500 cycles at 4 C	88.5% capacity retention after stitching 120 cycles	[11]
1 M $ZnSO_4$ CWK biogel	$NaV_3O_8·1.5H_2O$	1.7 mS·cm^{-1}	206.4 mAh·g^{-1} at 0.1 A·g^{-1}	180.8 mAh·g^{-1} after 500 cycles at 1 A·g^{-1}	-	[12]
2 M $ZnSO_4$ + 0.2 M $MnSO_4$ Alg-Zn	α-MnO_2/CNT	18.3 mS·cm^{-1}	~350 mAh·g^{-1} at 0.05 A·g^{-1}	~300 mAh·g^{-1} after 100 cycles at 0.05 A·g^{-1}	-	[13]
2 M $ZnSO_4$ + 0.2 M $MnSO_4$ PZHE	VS_2	32 mS·cm^{-1}	~140 mAh·g^{-1} at 0.2 A·g^{-1}	~90 mAh·g^{-1} after 500 cycles at 1.0 A·g^{-1}	-	[14]
0.5 M $ZnSO_4$ + 0.5 M Li_2SO_4 GHE	$LiMn_2O_4$	6.15 mS·cm^{-1}	110.2 mAh·g^{-1} at 0.02 A·g^{-1}	~100 mAh·g^{-1} after 100 cycles at 0.025 A·g^{-1}	-	[15]
0.25 M $ZnSO_4$ + 0.25 M Li_2SO_4 PHE	$LiFePO_4$	6.33 mS·cm^{-1}	169 mAh·g^{-1} at 0.1 C	152 mAh·g^{-1} after 300 cycles at 0.5 C	~90% capacity retention after bending 1000 cycles	[16]
1 M NaCl + 1 M $ZnSO_4$ sodium alginate	CuHCF/CNT	9.32 mS·cm^{-1}	260 mAh·g^{-1} at 0.5 A·g^{-1}	~215 mAh·g^{-1} after 450 cycles at 1 A·g^{-1}	-	[17]

References

[1] a) Y. Ding, Y. Wen, C. Wu, P. A. van Aken, J. Maier, Y. Yu, *Nano Lett.* **2015**, 15, 1388-1394; b) M. Liao, J. Wang, L. Ye, H. Sun, Y. Wen, C. Wang, X. Sun, B. Wang, H. Peng, *Angew. Chem. Int. Ed.* **2020**, 59, 2273-2278.
[2] Y. Liu, Y. Zhao, H. Zhang, X. Li, P. Liang, X. Zhang, J. Xu, *Macromolecules* **2004**, 37, 6362-6369.
[3] X. Wang, S. Zheng, F. Zhou, J. Qin, X. Shi, S. Wang, C. Sun, X. Bao, Z. Wu, *Natl. Sci. Rev.* **2019**, 7, 64-72.
[4] S. Zheng, H. Wang, P. Das, Y. Zhang, Y. Cao, J. Ma, S. Liu, Z. Wu, *Adv. Mater.* **2021**, 33, 2005449.
[5] H. Lu, J. Hu, L. Wang, J. Li, X. Ma, Z. Zhu, H. Li, Y. Zhao, Y. Li, J. Zhao, B. Xu, *Adv. Funct. Mater.* **2022**, 32, 2112540.
[6] Y. Zhou, S. Wang, J. Peng, Y. Tan, C. Li, F. Y. C. Boey, Y. Long, *Joule* **2020**, 4, 2458-2474.
[7] S. Zhang, N. Yu, S. Zeng, S. Zhou, M. Chen, J. Di, Q. Li, *J. Mater. Chem. A* **2018**, 6, 12237-12243.
[8] X. Pu, D. Zhao, C. Fu, Z. Chen, S. Cao, C. Wang, Y. Cao, *Angew. Chem. Int. Ed.* **2021**, 60, 21310-21318.
[9] Z. Chen, P. Wang, Z. Ji, H. Wang, J. Liu, J. Wang, M. Hu, Y. Huang, *Nano-Micro Lett.* **2020**, 12, 75.
[10] H. Li, Z. Liu, G. Liang, Y. Huang, Y. Huang, M. Zhu, Z. Pei, Q. Xue, Z. Tang, Y. Wang, B. Li, C. Zhi, *ACS Nano* **2018**, 12, 3140-3148.
[11] D. Wang, H. Li, Z. Liu, Z. Tang, G. Liang, F. Mo, Q. Yang, L. Ma, C. Zhi, *Small* **2018**, 14, 1803978.
[12] Y. Shao, J. Zhao, W. Hu, Z. Xia, J. Luo, Y. Zhou, L. Zhang, X. Yang, N. Ma, D. Yang, Q. Shi, J. Sun, L. Zhang, J. Hui, Y. Shao, *Small* **2022**, 18, 2107163.
[13] Y. Tang, C. Liu, H. Zhu, X. Xie, J. Gao, C. Deng, M. Han, S. Liang, J. Zhou, *Energy Stor. Mater.* **2020**, 27, 109-116.
[14] K. Leng, G. Li, J. Guo, X. Zhang, A. Wang, X. Liu, J. Luo, *Adv. Funct. Mater.* **2020**, 30, 2001317.
[15] Q. Han, X. Chi, S. Zhang, Y. Liu, B. Zhou, J. Yang, Y. Liu, *J. Mater. Chem. A* **2018**, 6, 23046-23054.
[16] J. Zhao, K. K. Sonigara, J. Li, J. Zhang, B. Chen, J. Zhang, S. S. Soni, X. Zhou, G. Cui, L. Chen, *Angew. Chem. Int. Ed.* **2017**, 56, 7871-7875.
[17] W. Pan, Y. Wang, X. Zhao, Y. Zhao, X. Liu, J. Xuan, H. Wang, D. Y. C. Leung, *Adv. Funct. Mater.* **2021**, 31, 2008783.

Author Contributions

H. Peng and B. Wang conceived and directed the research project. P. Li and M. Liao designed the experiments, analyzed the data, and wrote the manuscript. S. Cui, L. Ye, Y. Yang, and C. Wang helped with characterizations. S. Cui and J. Li provided helpful advice on the working mechanism analysis. All authors discussed the results and commented on the manuscript.